POLITECNICO DI TORINO
Repository ISTITUZIONALE

Strain-based fracture response of X80 steel pipe welded girth based on constraint-modified J-R curves: from SENT specimen to full-scale pipe

Original
Strain-based fracture response of X80 steel pipe welded girth based on constraint-modified J-R curves: from SENT specimen to full-scale pipe / Li, Z., Gong, B., Lacidogna, G., Deng, C., Wang, D.. - In: ENGINEERING FRACTURE MECHANICS. - ISSN 0013-7944. - ELETTRONICO. - 258:(2021), p. 108114. [10.1016/j.engfracmech.2021.108114]

Availability:
This version is available at: 11583/2941172 since: 2021-11-29T11:08:36Z

Publisher:
Elsevier

Published
DOI:10.1016/j.engfracmech.2021.108114

Terms of use:

This article is made available under terms and conditions as specified in the corresponding bibliographic description in the repository

Publisher copyright
Elsevier postprint/Author's Accepted Manuscript

© 2021. This manuscript version is made available under the CC-BY-NC-ND 4.0 license
http://creativecommons.org/licenses/by-nc-nd/4.0/.The final authenticated version is available online at:
http://dx.doi.org/10.1016/j.engfracmech.2021.108114

(Article begins on next page)

28 June 2026

Strain-based fracture response of X80 steel pipe welded girth based on constraint-modified *J-R* curves: from SENT specimen to full-scale pipe

Ziwei Li[a], Baoming Gong[a*], Giuseppe Lacidogna [b], Caiyan Deng[a]

[a] *Department of Materials Science and Engineering, Tianjin University, Road Weijin 92, 300072 Tianjin, China*
[b] *Department of Structural Engineering, Geotechnics and Building, Politecnico di Torino, Corso Duca degli Abruzzi 24, 10129 Torino, Italy*

*The correspondence E-mail: gongbm@tju.edu.cn

Abstract

In the study, a methodology is proposed based on the SENT experiments and crack-tip constraint theory to determine the tensile strain capacity of a flawed pipe welded girth. Firstly, the clamped SENT specimens with a wide range of geometrical variations are conducted to determine the *J-R* curves. The constraint-quantified *J-R* curves are then formulated using the out-of-plane extension of bending modified *J-Q* theory, and show well match with the experimental data. Finally, the extrapolated resistance curves from SENT to full-scale pipes are used for strain-based fracture assessment of a flawed pipeline. A relatively good agreement in terms of TSC between the present work and ExxonMobil's strain-based engineering critical assessment approach can be achieved.

.

Keywords: Crack-tip constraints; *J*-R curves; SENT.

1 Introduction

The transportation of Oil and Gas in harsh conditions should be considered at the design stage of pipelines. Recently, the strain-based design (SBD) method [1–5] is being increasingly used to address the deployment and subsequent operation of pipelines, such as offshore pipe laying and large ground movements imposed on onshore pipelines. Therefore, fracture toughness in terms of the *J*-integral (*J*)–*R* or crack tip opening displacement (CTOD)–*R* curve is a critical parameter in the strain-based integrity assessment of steel pipeline [6–9]. Furthermore, due to the similarity in the crack-tip stress and strain fields between the SE(T) specimen and the surface-flawed full-scale pipe under longitudinal tension and/or internal pressure, the fracture toughness determined from the SE(T) specimen can lead to more accurate strain-based design of pipelines with surface cracks. Therefore, the development of experimental procedures of the standard single-edge tension (SE(T)) specimen and the correlation of fracture behaviors between the standard specimen and the full-scale pipe has gained significant interest during the last decade.

Although the low-constraint SENT specimen is not recommended in ISO and ASTM standards so far, DNV proposed their SENT test method DNV-RP-F108 [10] in 2006, which is further improved by TWI and designated as BS 8571 [11] in 2014. DNV-RP-F108 and BS 8571 adopt the multiple specimen (a minimum of six specimens) method for *J*-*R* curve in pin-loaded or clamped SENT specimen. The specimen thickness is $B=2W$, the distance between the two grips is $H=10W$, and the pre-cracked length is in the range of $0.2<a/W<0.5$. Similar to ASTM E1820 [12], CanMet [13] developed a single specimen method based on the unloading compliance technique for clamped SENT specimen for *J*-*R* curve or CTOD-*R* curve determination. The specimen width $W=B$, the clamping distance $H=10W$, and the pre-fatigued crack size is in the range of $0.1<a/W<0.7$, and a total side groove of 15% of thickness is recommended. Based on the classical rigid rotation assumption for the shallow crack in BS 7448 [14] and ISO 12135 [15], ExxonMobil [16] developed a single specimen method for CTOD-*R* curve testing using a double clip gage arrangement, where the

homothetic triangle directly obtains both CMOD and CTOD. In the ExxonMobil method, the clamped SENT specimens have W=B and H=10W, and the initial crack length is $0.25 < a_0/W < 0.35$, and the total side groove of 10% of thickness is recommended. Cravero and Ruggieri [17,18] also developed a single specimen method to measure J-R curves for SENT specimens in homogenous materials and welds. Their test procedure is similar to ASTM E1820 and CanMet procedures with the unloading compliance technique. Denys et al. [19] also used the double-clip gage arrangement to determine δ-R curves for the clamped SENT specimens with the definition of CTOD based on the 90 intercept method starting from the original crack tip.

As discussed previously, only few testing practice procedures for SE(T) specimens and very limited number of geometrical sizes combinations are available in the literature [10,11,20]. Among them, most of the standardized SE(T) specimens are a rectangular dimension B equals to W or 2W, where W is referred to the direction of crack propagation and B represents the direction parallel to the crack front [10,11]. A wide range of geometrical sizes including different crack depth and thickness ratios have not yet been studied, and the geometry, size and loading dependence of the crack growth resistance in the SE(T) test are still not exhausted. The so-called ‘transferability’ problem between the laboratory specimens recommended in the SENT test procedures and the practical high-pressure pipe systems has raised an issue on correcting the resistance curves determined using standard SENT specimens for pipelines.

Recently, several researchers have experimentally and numerically studied the varying constraint effects on fracture toughness using SENT specimens with non-standardized geometrical configurations. The additional in-plane and out-of-plane crack tip constraint parameters characterizing the deviation of the local stress field have been introduced to allow a transfer of toughness data from small to large structures and from one geometry to another [21–23]. Liu et al. [21] found out that both in-plane and out-of-plane constraints can affect the J-R curves and there is strong interaction between both effects. Li et al. [24] discovered that fracture toughness decreases with increasing specimen thickness until B/W=4, indicating a strong influence of

out-of-plane constraint. Wang et al. [25]investigated the impact of specimen dimensions on the in-plane and out-of-plane constraints and concluded that interactions between both constraints can be indicated based on FE analyses. Both experimental and numerical investigation show that the crack initiation toughness and propagation resistance decreases noticeably as specimen thickness increases, and the out-of-plane constraint and its coupling with the in-plane constraint effects on the ductile tearing can be not trivial. Moreover, for the practical high-pressure piping, the out-of-plane constraint along the circumferential direction may significantly affect fracture toughness, which deserves more attention in the structural assessment and design [26–28].

In the study, the primary target is to explore a full-scale pipe girth weld fracture prediction methodology based on the laboratory size SENT testing and crack tip constraint correction theory. Firstly, a wide range of geometrical clamped SENT specimens sizes with different crack depth and thickness ratios is conducted to determine the *J-R* curves. Considering opening- and bending-dominated ligament deformations, the out-of-plane extension of bending modified *J-Q* theory is used to construct the constraint-quantified *J-R* curves from the different standardized SENT tests to the full-scale pipe with surface crack. Finally, the obtained tear resistance of full-scale pipe is used for fracture assessment in terms of tensile strain capacity (TSC), and the comparison is performed against the results by ExxonMobil.

2 Overview of crack-tip constraint theories

In the work, three constraint parameters are considered for the clamped SENT, i.e. Q_m, Q_z and A_2. Compact outlines on how they are determined and their application to describe the crack-tip constraints are given as follows.

2.1 The J-A_2 theory

The J-A_2 theory is proposed by Yang et al. [29] and Chao et al. [30] to characterize the crack-tip fields and constraint levels for all specimens considered, and the three-term asymptotic stress field is given as:

$$\frac{\sigma_{ij}}{\sigma_0} = A_1((\frac{r}{L})^{s_1}\tilde{\sigma}_{ij}^{(1)}(\theta,n) + A_2(\frac{r}{L})^{s_2}\tilde{\sigma}_{ij}^{(2)}(\theta,n) + A_2^2(\frac{r}{L})^{s_3}\tilde{\sigma}_{ij}^{(3)}(\theta,n)) \quad (1)$$

where the stress angular functions $\tilde{\sigma}_{ij}^{(k)}(\theta)$ and the stress power exponents s_k only depend on the hardening exponent n [31]; L is a characteristic length parameter and equal to 1 mm in the study; A_1 is a variable from HRR fields and can be given by:

$$A_1 = (\frac{J}{\alpha\varepsilon_0\sigma_o I_n L})^{-s_1} \quad (2)$$

2.2 The bending modified J-Q theory

In order to describe the crack tip stress fields under large scale yielding and the influence of global bending stress, Zhu et al. developed the parameter Q_m [32]:

$$Q_m = [\frac{J}{\alpha\varepsilon_0\sigma_0 I_n L}]^{-\frac{1}{n+1}} \times (\frac{\sigma_{\theta\theta}^{FEA}(r,0) - \sigma_{\theta\theta}^{HRR}(r,0)}{\sigma_0} + \frac{CMr}{\sigma_0 b^3}) \text{ at } r = 2J/\sigma_0 \quad (3)$$

where I_n is the integration constant from HRR fields and has been calculated by Shih [33] and M can be calculated using the applied stress：

$$M = \frac{\sigma^{\infty} aW}{2} \quad (4)$$

Moreover, C is a load-related coefficient and can be determined through the two-point matching method as follow:

$$C = \frac{\sigma_0 b^3}{M(r_2 - r_1)} \left\{ \begin{array}{l} [\frac{J}{\alpha\varepsilon_0\sigma_0 I_n L}]^{\frac{1}{n+1}} \times ((\frac{L}{r_2})^{\frac{1}{n+1}} - (\frac{L}{r_1})^{\frac{1}{n+1}})\sigma_{\theta\theta}(0,n) \\ -(\frac{\sigma_{\theta\theta}^{FEA}(r_2,0)}{\sigma_0} - \frac{\sigma_{\theta\theta}^{FEA}(r_1,0)}{\sigma_0}) \end{array} \right\} \quad (5)$$

In the equation, $\sigma_{\theta\theta}^{FEA}(r_1,0)$ and $\sigma_{\theta\theta}^{FEA}(r_2,0)$ are the opening stresses determined at two points where r=r_1 and r=r_2 through FEA. The bending-modified *J-Q* solution has been reported to describe the in-plane constraints with being both distance- and load-independence [34].

2.3 The out-of-plane extension of bending modified J-Q theory

Considering the out-of-plane constraint parameter, T_z [35,36], Gong et al. [34] proposed a modified solution of the *J*-*Q* theory to describe the out-of-plane constraint effect of the SE(T) specimens. The out-of-plane stress is proportional to the sum of two in-plane components:

$$\sigma_{zz}(r,0) = (\sigma_{xx}(r,0) + \sigma_{yy}(r,0)) \times T_z \tag{6}$$

Thus, the out-of-plane stress can be expressed as

$$\frac{\sigma_{zz}}{\sigma_0} = \frac{\sigma_{zz}^{FEA}}{\sigma_0} + [\frac{J}{\alpha\varepsilon_0\sigma_0 I_n L}]^{\frac{1}{n+1}} \times Q_z - \frac{C^{'}Mr}{\sigma_0 b^3} \tag{7}$$

where σ_{zz}^{HRR} is the HRR stress at *z*-direction and *C*' is the linearization factor. The calculation of both Q_z and *C*' are similar to Eq. (3) and Eq. (5):

$$C' = \frac{b^3}{M(r_2 - r_1)} \times [\sigma_{zz}^{HRR}(r_2,0) - \sigma_{zz}^{HRR}(r_1,0) - (\sigma_{zz}^{FEA}(r_2,0) - \sigma_{zz}^{FEA}(r_1,0))] \tag{8}$$

$$Q_z = [\frac{J}{\alpha\varepsilon_0\sigma_0 I_n L}]^{-\frac{1}{n+1}} \times (\frac{\sigma_{zz}^{FEA} - \sigma_{zz}^{HRR}}{\sigma_0} + \frac{C'Mr}{\sigma_0 b^3}) \text{ at } r = 2J/\sigma_0 \tag{9}$$

It has been numerically demonstrated [34] that the out-of-plane extension of bending modified *J*-*Q* theory can characterize the out-of-plane constraint of SE(T) specimens with distance-independence, load-independence. Experimentally, the out-of-plane constraint loss is demonstrated by the parameter Q_z as *B/W* is less than 2 as reported in [24].

3 Experimental procedure and results

3.1 Material property and specimen geometry

The material is API X80 pipeline steel with girth weld. All specimens were cut longitudinally from pipeline with an outer diameter of 1219 mm and a thickness of 18.4 mm. The tensile properties of both base metal and weld joints were measured using the standard round bars with a 6 mm gauge diameter [37]. The yield stress is 587 MPa for the base metal and 608 MPa for weld metal.

For API X80 base metal and its weld, the stress-strain curves can be fitted by the Ramberg-Osgood

power-law equation:

$$\frac{\varepsilon}{\varepsilon_0}=\frac{\sigma}{\sigma_0}+\alpha(\frac{\sigma}{\sigma_0})^n \tag{10}$$

where $\varepsilon_0=\sigma_0/E$ is the yield strain, σ_0 is the yield stress, n is the hardening exponent, and α is a constant. These parameters for both X80 base metal and weld joints are listed below in Table 1.

Table 1
Material parameters for both base metal and weld metal.

	E/(GPa)	v	σ_0/(MPa)	n	α
X80 Base metal	207	0.3	587	10	2.56
X80 Weld metal	207	0.3	608	5	0.90

The clamped SE(T) specimen of X80 weld metal configuration is illustrated in Fig. 1. A wide range of geometrical dimensions are considered and listed in Table 2. Side grooves with a 0.5 mm root radius, 7.5% thickness reduction at each side and an angle of 45° are introduced to all specimens [11]. In the following sections, the test data of SE(T)-1 to SE(T)-7 is used to construct the Q_m-Q_z and J-A_2 constraint-modified J-R curves, while the test data of SE(T)-8 to SE(T)-10 is used for validation.

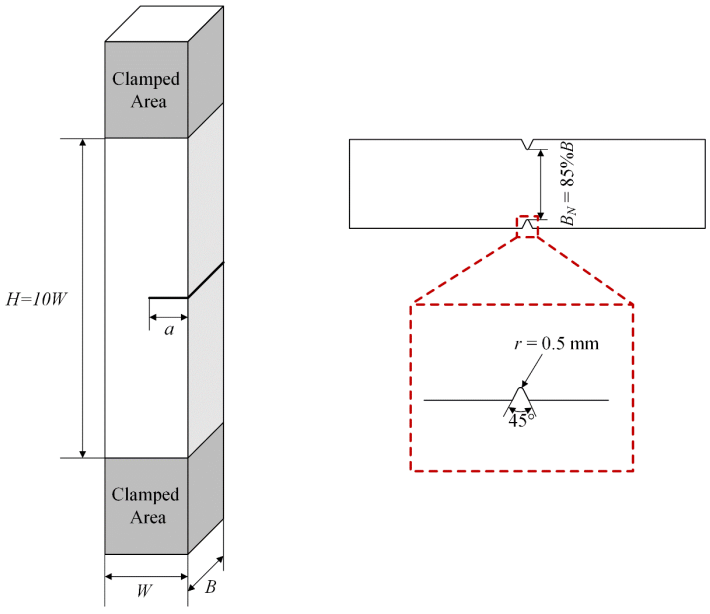

Fig. 1 SE(T) test specimen configuration.

Table 2 Dimensions of the SE(T) specimens.

Specimen No.	W/(mm)	B/W	a_0/W	B_N/(mm)
SE(T)-1	18	0.5	0.40	7.65
SE(T)-2	18	1.0	0.40	15.30
SE(T)-3	18	2.0	0.40	30.60
SE(T)-4	18	3.0	0.40	45.90
SE(T)-5	18	1.0	0.20	15.30
SE(T)-6	18	1.0	0.50	15.30
SE(T)-7	18	1.0	0.60	15.30
SE(T)-8	17	1.0	0.25	14.45
SE(T)-9	18	1.0	0.30	15.30
SE(T)-10	17	1.0	0.35	14.45

3.2 SE(T) test procedures

The SE(T) tests were performed using an MTS E64 testing machine with a 1000 kN loading frame. All specimens were clamped and loaded under displacement-control mode with a crosshead velocity of 0.01 mm/s at room temperature. Only one clip gauge was used to measure the crack mouth opening displacement (CMOD) as suggested in ASTM E1820-20b [12]. During the test, the Unloading Compliance (UC) method [13,38,39] was adopted to determine the crack length. The specimens were initially unloaded and reloaded within the range of 0.1 to 0.5 $P_y = (W - a_0)B_N\sigma_f$ to pre-check the setting of the clip gauge. Then, the unload/load cycles were performed based on a fixed CMOD interval. Finally, in order to obtain a sufficient amount of ductile crack extension, the tests were not stopped until the current load is below 20% of the maximum load.

3.3 Evaluation of J-R curves

In the study, *J-R* curves are determined according to CanMet [13]. The *J*-integral can be divided into the elastic and the plastic components[12]:

$$J_{(i)} = J_{el(i)} + J_{pl(i)} \tag{11}$$

and the elastic part $J_{el(i)}$ can be given by LEFM as:

$$J_{el(i)} = \frac{(K_{(i)})^2(1-\upsilon^2)}{E} \tag{12}$$

where E is the Young's Modulus, v is the Poisson's ratio, $K_{(i)}$ is the stress intensity factor which can be expressed as

$$K_{(i)} = \frac{P_{(i)}}{\left(BB_N W\right)^{1/2}} F\left(\alpha\right) \tag{13}$$

In this equation, $\alpha = a/W$, $B_N = 85\%B$ is the net specimen thickness, and $F(\alpha)$ is directly related to α through

$$F(\alpha) = \frac{\alpha^{1/2}}{(1+2\alpha)(1-\alpha)^{3/2}} \begin{bmatrix} 1.9873 + 0.7422\alpha + 11.188\alpha^2 - 45.82\alpha^3 \\ +100.49\alpha^4 - 120.3\alpha^5 + 51.488\alpha^6 \end{bmatrix} \tag{14}$$

The plastic component $J_{pl(i)}$ is defined by

$$J_{pl(i)} = \left[J_{pl(i-1)} + \left(\frac{\eta_{CMOD(i-1)}}{b_{(i-1)}} \right) \left(\frac{A_{pl(i)} - A_{pl(i-1)}}{B_N} \right) \right] \cdot \left[1 - \gamma_{LLD(i-1)} \left(\frac{a_{(i)} - a_{(i-1)}}{b_{(i-1)}} \right) \right] \tag{15}$$

where the incremental plastic area $A_{pl(i)}$-$A_{pl(i-1)}$, the plastic factor $\eta_{CMOD(i)}$ and the geometry factor $\gamma_{LLD(i)}$ can be given as:

$$\eta_{CMOD(i)} = \sum_{t=0}^{10} \phi_t \left(\frac{a_i}{W}\right)^t \tag{16}$$

$$\gamma_{LLD(i)} = \eta_{LLD(i)} - 1 - \left(1 - \frac{a_i}{W}\right) \frac{\eta'_{LLD(i)}}{\eta_{LLD(i)}} \tag{17}$$

$$\eta_{LLD(i)} = \sum_{t=0}^{10} \psi_t \left(\frac{a_i}{W}\right)^t \tag{18}$$

$$\eta'_{LLD(i)} = \sum_{t=0}^{10} t \cdot \psi_t \left(\frac{a_i}{W}\right)^{t-1} \tag{19}$$

The constants ϕ_t, ψ_t for iterative values of t are given in Table 3.

The instantaneous crack length a_i is evaluated from the rotation corrected CMOD compliance as follow

$$a_i = \sum_{t=0}^{9} r_t (u_i)^t \tag{20}$$

$$u_i = \frac{1}{\sqrt{B_e C_{c(i)} E} + 1} \tag{21}$$

The value of the geometrical function r_t is also given in Table 3. $B_e = B - (B - B_N)^2 / B$ is the effective specimen thickness, and $C_{c(i)}$ is the rotation corrected compliance

$$C_{c(i)} = \frac{C_i}{1 - 0.165 \frac{a_0}{W} \left(\frac{P_{(i)}}{P_y} \right)} \tag{22}$$

The original compliance C_i is defined as reciprocal of the slope of the P versus CMOD curve at each unload/load cycle. $P_{(i)}$ is the maximum load at the same cycle, and P_y is the limit load. Then the crack extension, Δa_i, at a particular unload/load cycle can be determined through

$$\Delta a_i = a_i - a_{oq} \tag{23}$$

where a_{oq} is the revised initial crack depth determined based on the standard ASTM E1820-20b [12].

Table 3 Values of constants ϕ_t, ψ_t and r_t.

t	0	1	2	3	4	5
ϕ_t	1.000	-1.089	9.519	-48.572	109.225	-73.116
ψ_t	-0.880	15.190	-35.440	18.644	18.399	-1.273
r_t	2.044	-15.732	73.238	-182.90	175.653	60.93

t	6	7	8	9	10
ϕ_t	-77.984	38.487	101.401	43.306	-110.77
ψ_t	-12.756	-12.20	-4.447	5.397	14.187
r_t	-114.00	-113.0	8.545	142.84	

3.4 Experimental *J-R* curve

The *J-R* curves for API X80 girth weld specimens tested in the work are shown in Fig. 2(a) and Fig. 2(b). The experimental *J-R* curves of specimens with thickness ratio *B/W* =1, *a/W* ratio from 0.20 to 0.60 is plotted in Fig. 2(a). It can be found that crack depth ratios have remarkable influence on *J-R* curves. Fig. 2(b) shows *J-R* curves for different thickness ratios *B/W*=0.5, 1.0, 2.0 and 3.0 with the fixed crack depth ratios (*a/W*=0.4),

and there exists noticeable thickness effect on *J*-*R* curves. Similarly, Liu et al. [21] have observed that the out-of-plane constraint shows strong effect on *J*-*R* curves regardless of crack length, though the influence is great for shallow-cracked specimen and relatively small for deep-cracked specimen. Moreover, there exists interaction between the in-plane and out-of-plane constraints, and the higher in-plane constraints can intensify the out-of-plane constraint effect, resulting in an obvious change in out-of-plane constraint parameters, while a relatively low in-plane constraint can lead to insensitivity to out-of-plane constraints [40].

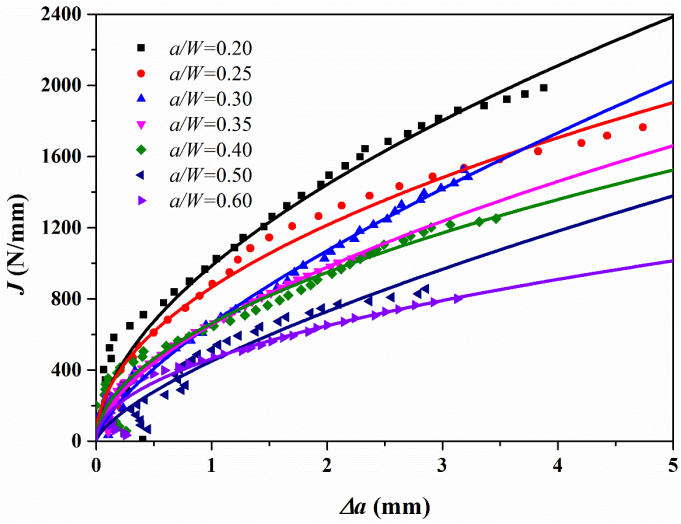

(a)

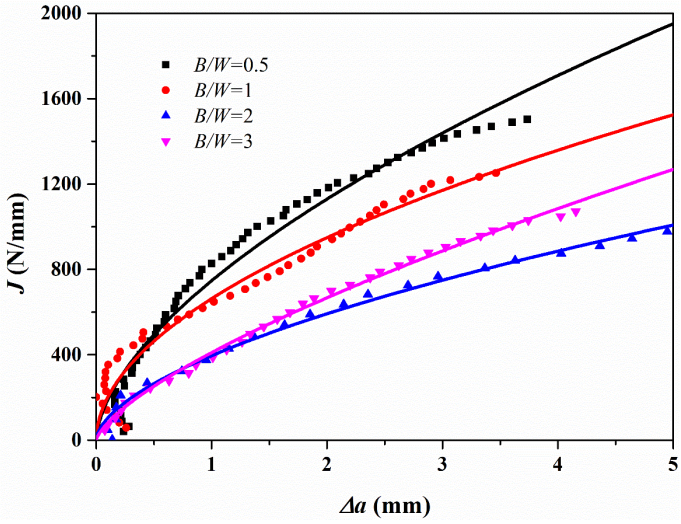

(b)

Fig. 2 Experimental *J*-*R* curves of X80 weld metal: *B*/*W*=1, different crack depths (a); a_0/W =0.4, different

thicknesses (b).

4 Calculation of crack-tip constraints

Three-dimensional FEA were conducted to obtain the values of crack-tip constraint parameters for both SE(T) specimens and full-scale pipeline with girth weld, and three favorable constraint parameters, i.e. Q_m, Q_z and A_2, are considered.

4.1 Constraint quantification analysis for SE(T) specimens

Finite element models of all specimens are constructed, and the geometry configurations are given in Table 2. Due to symmetry, only a quarter of the specimen is modelled using 8-node linear brick element (C3D8). The crack is assumed to be stationary in the analyses, and a root radius (ρ) of 2.5 μm was modelled to facilitate the convergence of the strain analysis (see Fig. 3). A refined spider-web mesh was applied to the blunt crack tip in Fig. 3. The constraint parameters are evaluated from the average stresses at θ=0° and crack tip distance from $r=J/\sigma_0$ to $r=5J/\sigma_0$, and the J-integral is chosen as 400 N/mm. For n=5, the HRR field variables, I_n, $\sigma_{rr}(0)$, and $\sigma_{\theta\theta}(0)$ are 5.22, 1.68, and 2.22, respectively [33]. The constraint results are given in Fig. 4. Fig.4 (a) shows that crack depth has a significant impact on in-plane constraints, all three constraint parameters generally rise as the crack depth increases. It can be seen from Fig.4 (b) that A_2 is insensitive to the out-of-plane constraints. However, For B/W = 0.5 and 1, the value of Q_z and Q_m rises as the specimen thickness increases. As the ratio increases to 2, Q_z and Q_m remain almost constant.

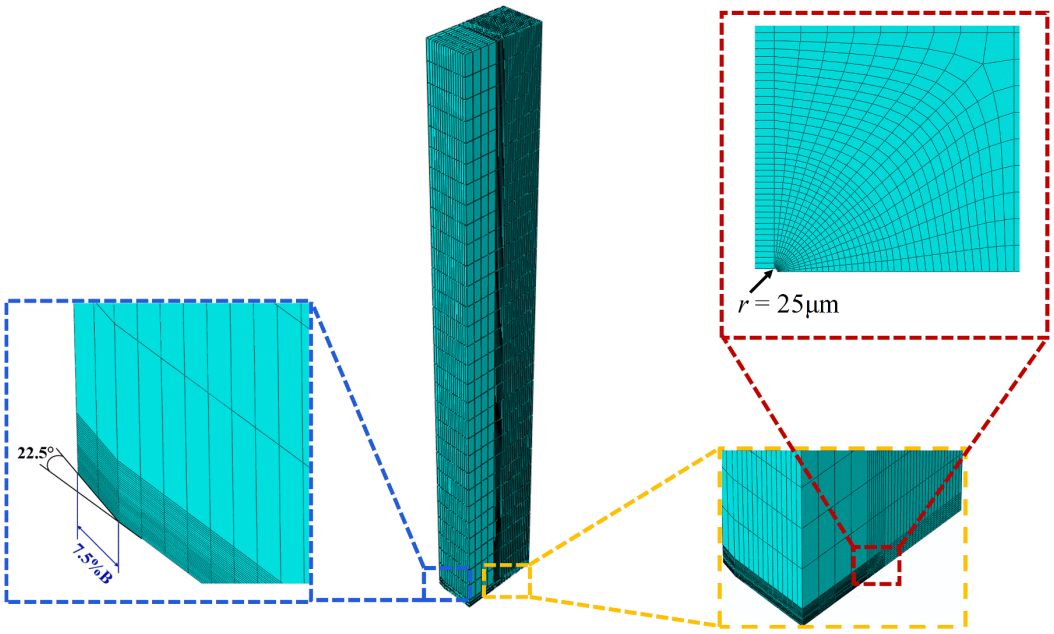

Fig. 3 The 3D finite element analysis model of SE(T) specimen.

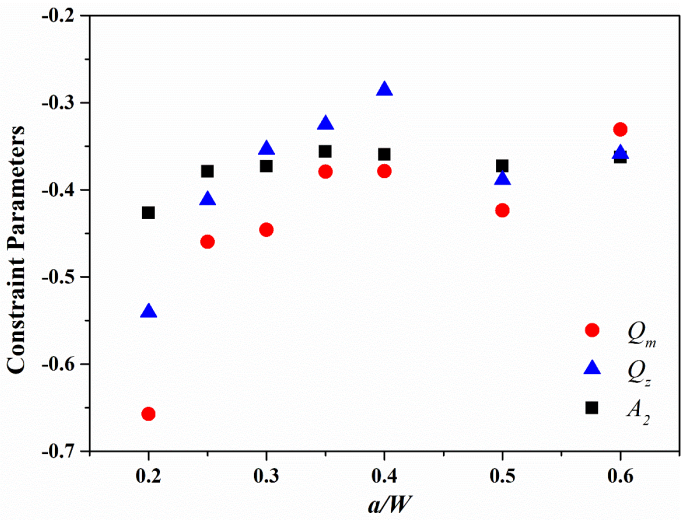

(a)

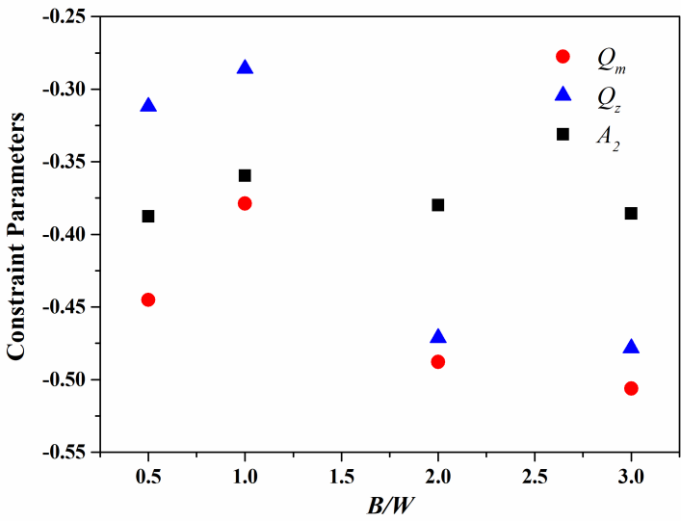

(b)

Fig. 4 Constraint parameters, Q_m, Q_z and A_2, determined through FEA: variations of in-plane constraints with crack depths (a); variations of out-of-plane constraints with specimen thicknesses (b).

4.2 Constraint analysis for full-scale pipe girth weld with a root surface crack

The geometrical configuration of the internal-cracked pipe with girth weld is demonstrated in Fig. 5, and the outer diameter D and the thickness t are 1219 mm and 18.4 mm. The half-length of the pipeline L is set to be 3657 mm, 3 times the outer diameter, and it has been proven that the adopted pipe length is long enough not to have an impact on the J-integral extracted from the FE simulation [41]. The internal crack is located at the weld centre line. A total of 36 models with different crack sizes are considered, and the crack dimensions are listed below in Table 4. Due to symmetry, only one fourth of the pipeline is considered in the finite element analysis and corresponding symmetry boundary conditions are adopted. Element type of 20-node brick element with reduced integration (C3D20R) is used. A blunt crack with a radius of 2.5 μm is adopted and a fine mesh is applied around the crack tip to improve the convergence (see Fig. 6). Tension was prescribed by displacement control at the un-cracked end of the pipeline through a reference point, which has already coupled with the nodes on the un-cracked end.

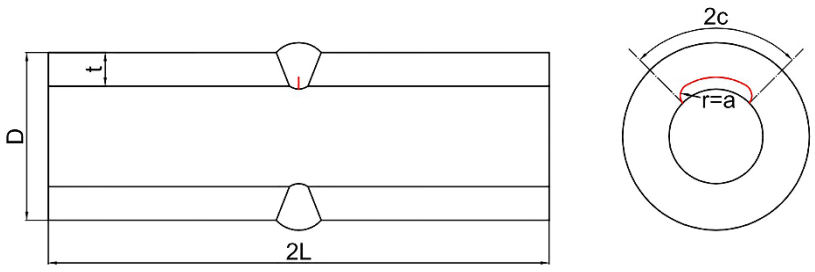

(a)

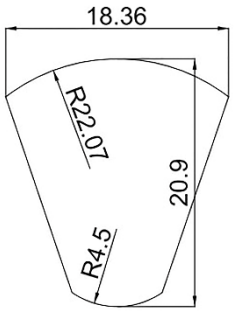

(b)

Fig. 5 Geometry of the welded pipe with an internal circumferential surface flaw (a); details of the weldment (b). (All dimensions are given in millimetre.)

Table 4 Crack dimensions for the pipeline models.

Crack length $2c/\pi D$	0.01	0.015	0.02	0.025	0.03
Crack depth a/(mm)	4.5	4.5	4.5	4.5	4.5
	5	5.5	5.5	5	5
	5.5	6	6	5.5	5.5
	6	6.5	6.25	6	6
	6.5	6.75	6.5	6.25	6.5
	6.75	7	7.5	6.5	7
	7.5	7.5		7	7.5
	8.25			7.5	

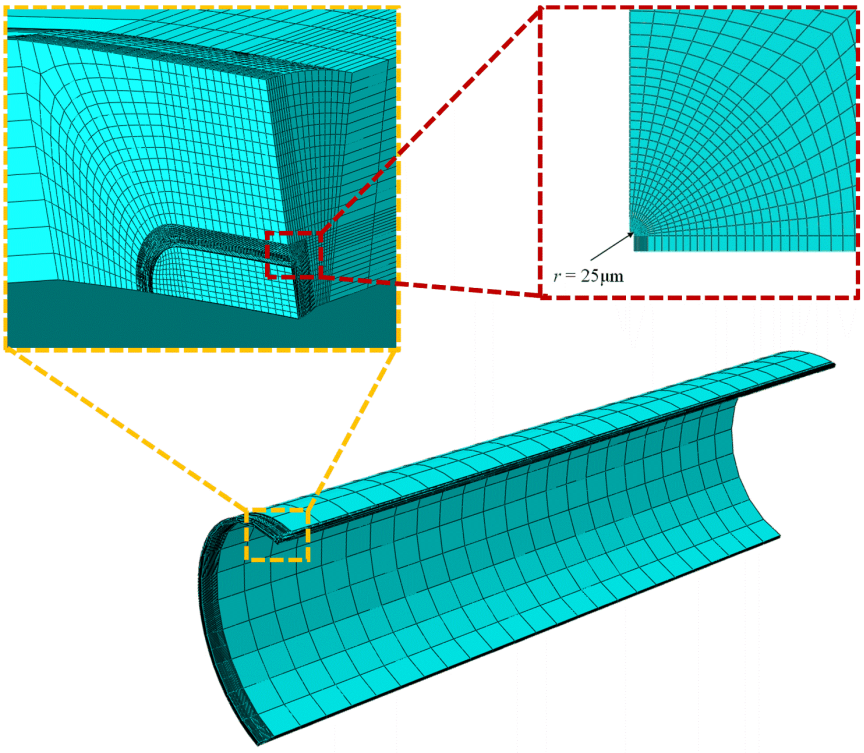

Fig. 6 The 3D finite element analysis model of the welded pipeline with an internal surface crack.

The values of Q_m and Q_z determined through FEA for the full-scale pipelines are given in Fig. 7. Fig. 7 shows that the crack lengths have a strong influence on the out-of-plane constraints of the pipeline, as the crack gets longer, the value of Q_z increases. On the contrary, the crack lengths have a negligible impact on the in-plane constraints, the value of Q_m remains almost constant. In order to simplify the further investigation, the value of Q_m will be taken as the average value, -0.595, as shown in Fig.7.

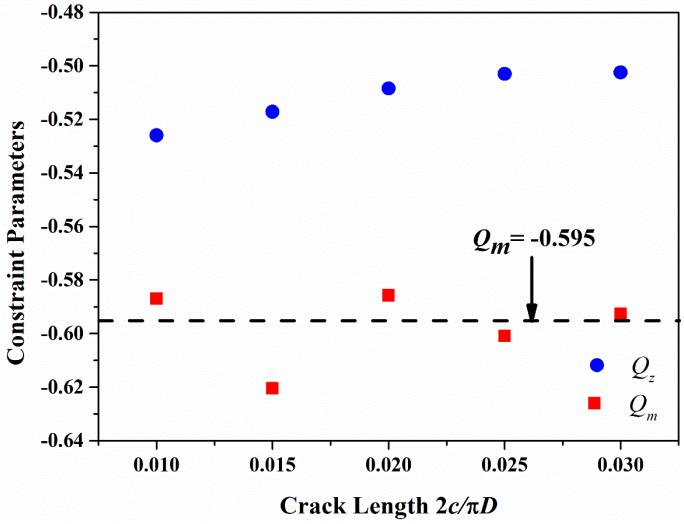

Fig. 7 Constraint parameters, Q_m and Q_z determined through FEA for the full-scale pipelines with the internal crack a_0=4.5 mm, $2c/\pi D$ =0.01, 0.015, 0.02, 0.025, 0.03.

5 Construction of constraint-modified *J-R* curves for SENT specimen

5.1 Q_m-Q_z constraint-modified J-R curve

The J -resistance curve can be approximated by a best-fit power-law relationship [12]:

$$J = c_1(\Delta a)^{c_2} \tag{24}$$

where the coefficients c_1 and c_2 are constraint-related constants. Considering the in-plane and out-of-plane constraint parameters in the work, Eq. (24) can be modified as:

$$J(\Delta a, Q_m, Q_z) = c_1(Q_m, Q_z)\cdot(\Delta a)^{c_2(Q_m, Q_z)} \tag{25}$$

As a result, the objective becomes the construction of the functional dependencies of c_1 and c_2 on Q_m and Q_z.

When the specimens exhibit much longer crack extension (Δa>2.0 mm), it is recommended to choose Δa larger than 2.0 mm to improve the fitting results [22]. Assuming that J-integral at two crack extensions lengths, Δa = 0.2 mm and 3.0 mm, are expressed by:

$$\begin{aligned} J_{0.2} &= c_1(Q_m, Q_z) \cdot 0.2^{c_2(Q_m, Q_z)} \\ J_{3.0} &= c_1(Q_m, Q_z) \cdot 3.0^{c_2(Q_m, Q_z)} \end{aligned} \tag{26}$$

Furthermore, the experimental data described in Section 3.4 were fitted to the following expression:

$$J = a + bQ_m + cQ_z + dQ_m^{\,2} + eQ_z^{\,2}, \tag{27}$$

The fitted results are tabulated in Table 5 and presented in Fig. 8. Rearranging Eq. (26), the values of c_1 and c_2 with respect to different Q_m and Q_z can be determined, and the results were fitted by:

$$\begin{aligned} c_1 &= a + bQ_m + cQ_z + dQ_m^{\,2} + eQ_z^{\,2} \\ c_2 &= a + bQ_m + cQ_z + dQ_m^{\,2} + eQ_z^{\,2} \end{aligned} \tag{28}$$

The results are given in Table 5 and the fitted surface are shown in Fig. 9. By substituting Eq. (28) to Eq. (24), the constraint-modified J-R curve is obtained.

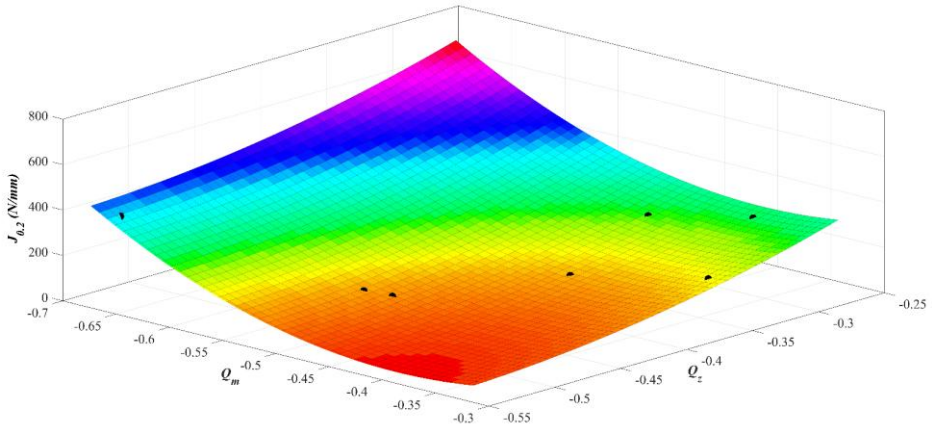

(a)

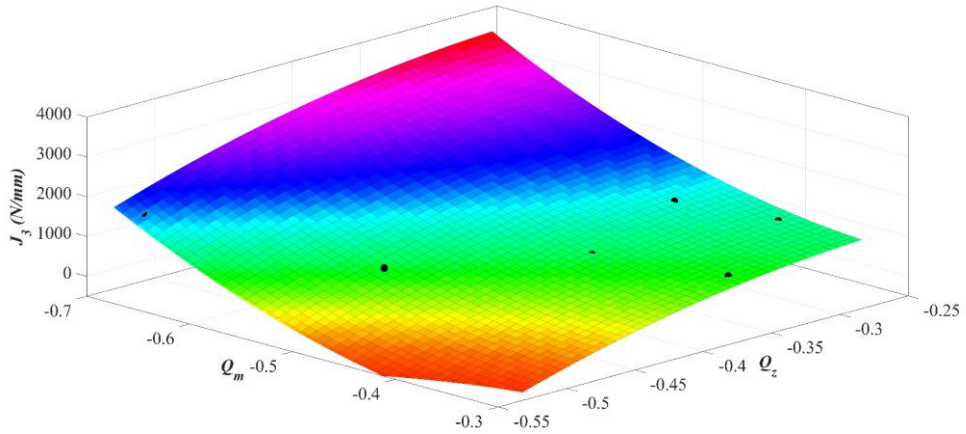

(b)

Fig. 8 The constructed three-dimension surface of J-Q_m-Q_z of API X80 weld joint at Δa = 0.2 mm (a); Δa=3.0 mm (b).

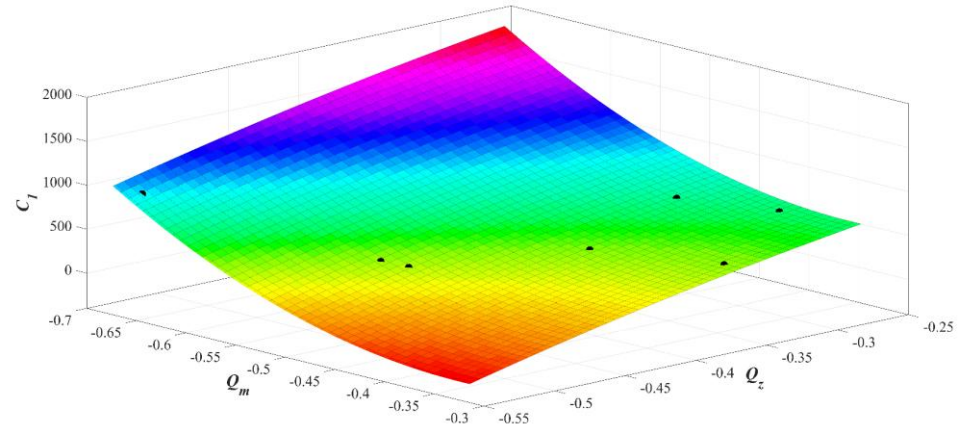

(a)

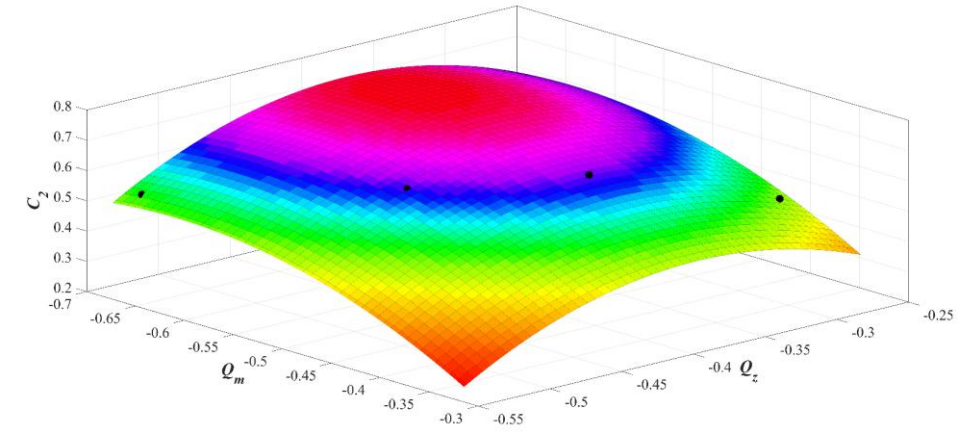

(b)

Fig. 9 The constructed three-dimension surfaces of c_1-Q_m -Q_z (a) *and* c_2-Q_m-Q_z (b) of API X80 weld joint.

Table 5 The fitting coefficients for $J_{0.2}$, J_3, c_1 and c_2.

	a	b	c	d	e
$J_{0.2}$	1709.54	3704.85	3226.01	4805.33	2737.89
J_3	1205.58	8755.92	-8409.53	16569.47	-18302.27
c_1	2124.31	6556.22	631.89	10164.85	-3005.69
c_2	-1.71	-3.88	-6.65	-3.17	-8.60

5.2 The J-A_2 constraint-modified J-R curves

Based on the methodology described by Chao and Zhu [23], the power law curve fitting parameters can be a function of the constraint parameters, A_2, and Eq. (24) can be expressed by:

$$J(\Delta a, A_2) = c_1(A_2) \cdot (\Delta a)^{c_2(A_2)} \tag{29}$$

To solve the two coefficients c_1 and c_2, two equations are established at two points of crack extension, Δa = 0.2 and 3.0 mm, using the same experimental data determined in Section 3.

$$\begin{aligned} J_{0.2} &= c_1(A_2) \cdot 0.2^{c_2(A_2)} \\ J_{3.0} &= c_1(A_2) \cdot 3.0^{c_2(A_2)} \end{aligned} \tag{30}$$

Fig. 10 demonstrates the relations between the values of J at Δa = 0.2 and 3.0 mm and the constraint parameter A_2. From this figure, two linear equations are fitted as follows:

$$\begin{aligned} J_{0.2} &= -2736.77A_2 - 794.90 \\ J_{3.0} &= -7069.08A_2 - 2079.00 \end{aligned} \tag{31}$$

Substituting Eq. (31) to Eq. (29) leads to the simultaneous equations for c_1 (A_2) and c_2(A_2), and numerical methods can be used to solve the equations. The resulting data points can later be fitted by:

$$\begin{aligned} c_1 &= -6710.68A_2 - 1973.91 \\ c_2 &= 0.48 - 0.43A_2 - 0.57A_2^{\,2} - 0.25A_2^{\,3} \end{aligned} \tag{32}$$

Substituting Eq. (33) into Eq. (24), the constraint-modified *J-R* curves based on the *J*-A_2 theory is obtained.

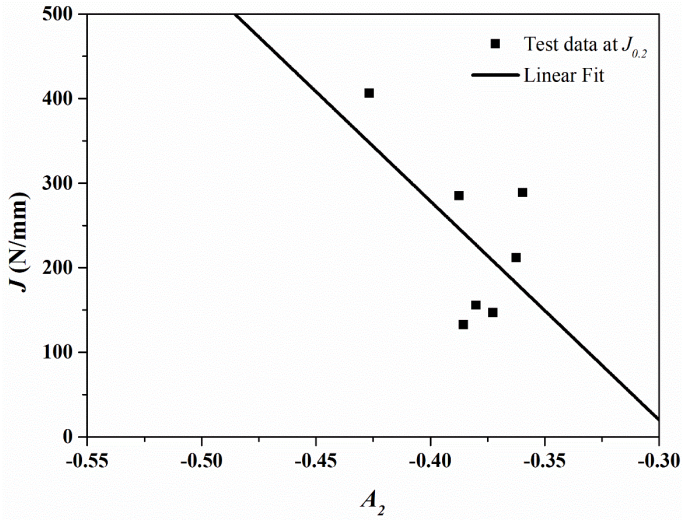

(a)

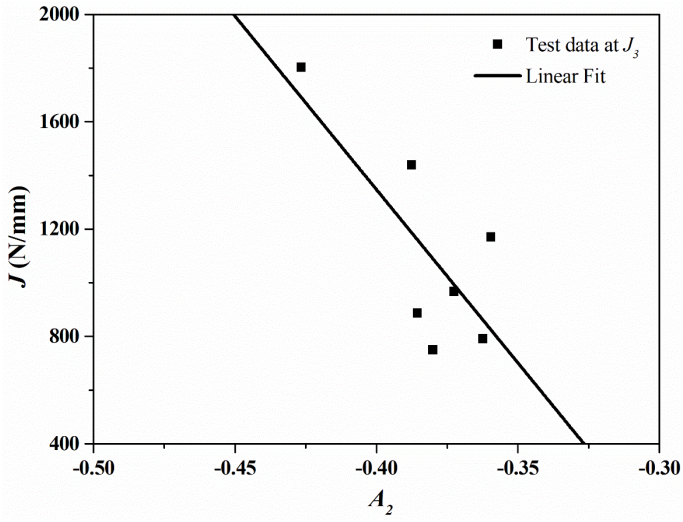

(b)

Fig. 10 Variations of the value of J at Δa = 0.2 mm with A_2 (a); variations of the value of J at Δa = 3.0 mm with A_2 (b).

5.3 Experimental Validation of the constructed J-R curve

In order to check the accuracy of the two constraint-modified *J-R* curve construction methods, three different SE(T) specimens are considered. The geometrical dimensions and experimental details are given in Table 2. For comparison, the experimental and the predicted *J-R* curves by both methods are plotted in Fig. 11 It is indicated in Fig. 11 that the prediction by the Q_m-Q_z constraint method match well with the experimental *J-R* curves, though the *J*-A_2 solution gives a better prediction than the Q_m-Q_z constraint method at a_0/W = 0.25. Moreover, the *J*-A_2 solution tends to underestimate the *J-R* curves with an average error of 30%

as the initial crack depth gets deeper, whilst the deviations based on Q_m and Q_z are less than 10%. In general, it can be found that the predicted *J*-*R* curves by the Q_m-Q_z constraint method can match well with the experimental data up to Δa =3.5 mm. Therefore, the proposed method can predict the crack resistance curve in a large range of crack growth with much more accuracy.

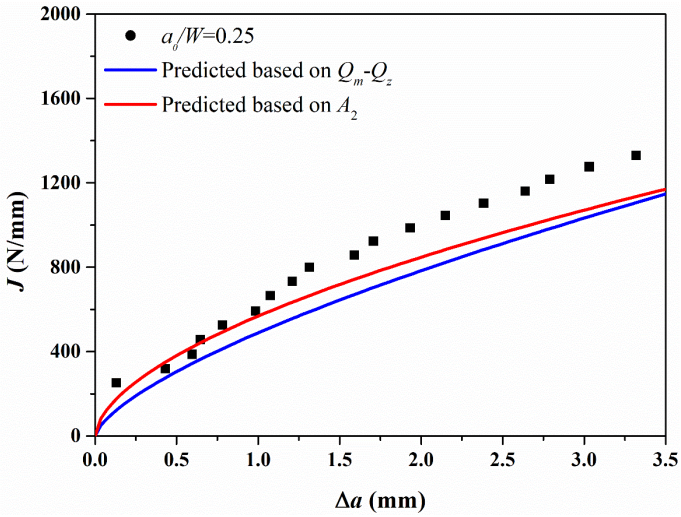

(a)

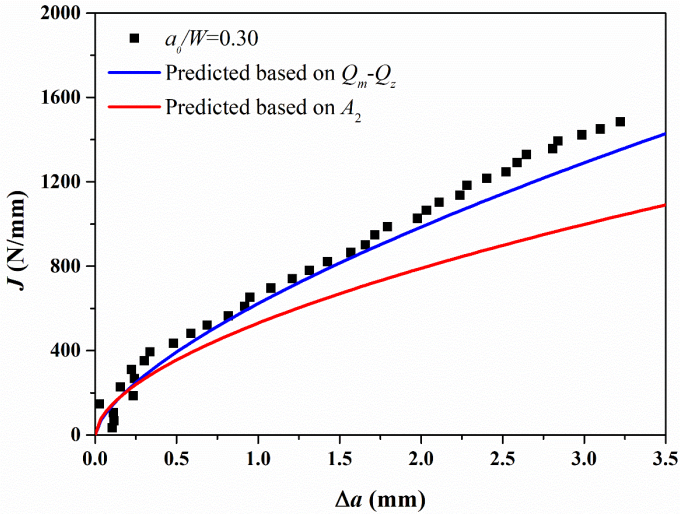

(b)

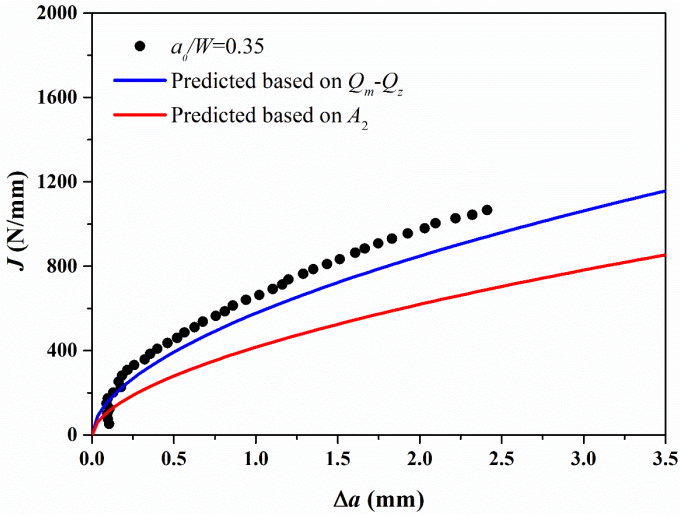

(c)

Fig. 11 Comparisons between the predicted *J-R* curves and the experimental ones when: a_0/W = 0.25 (a); a_0/W = 0.30 (b); a_0/W = 0.35 (c).

6 Constraint-modified *J-R* curves for full-scale girth weld

In order to illustrate the application of the constraint-modified *J-R* curves in engineering critical assessment (ECA), a scenario of a girth welded X80 pipeline with an internal surface crack under tension is considered here. The *J-R* curves of the full-scale pipeline are extrapolated based on the constraint correction Q_m-Q_z method in Sections 4.2 and the full-scale pipe constraint parameter Q_m and Q_z determined numerically in Fig. 7. Finally, the fracture assessment result based on the predicted *J-R* curves of the full-scale pipeline are compared against that by ExxonMobil strain-based engineering critical assessment approach.

6.1 Predicted J-R curves for the full-scale pipelines

More details on the pipelines considered here have already been given in Section 4.2. The predicted *J-R* curves for the full-scale cracked pipelines with the initial crack depth 4.5 mm, and five crack lengths are presented in Fig.12. It can be seen from Fig.12 that as the crack length gets longer, the predicted resistance curve becomes higher.

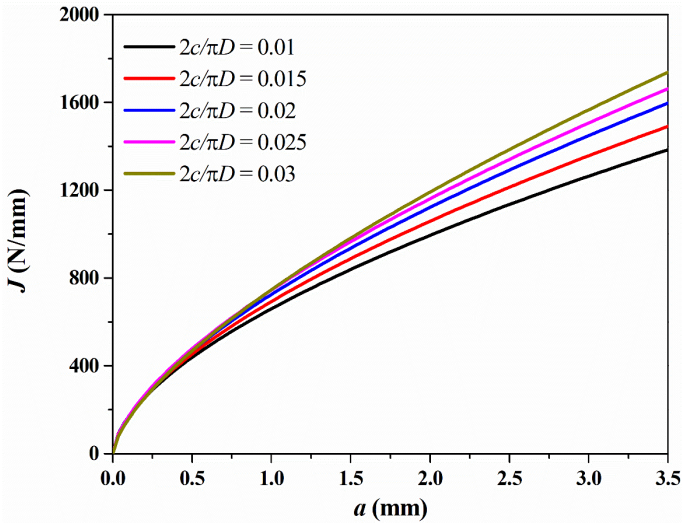

Fig. 12 The predicted *J*-*R* curves for the full-scale pipelines with the internal crack a_0=4.5 mm, $2c/\pi D$=0.01, 0.015, 0.02, 0.025, 0.03.

6.2 Assessment of the tensile strain capacity (TSC)

The tensile strain capacity (TSC) can be determined based on the tangent method procedure recommended by DNVGL-RP-F108 [10] where the crack driving force curves can be obtained numerically by 3D finite element fracture mechanics analyses and the crack resistance curve is determined by the constraint-modified scheme as discussed before. Then, the driving force curves at different strain and the resistance curve are plotted in the same diagram, and the strain level where the two curves are tangent at each other is taken as the tensile strain capacity, as demonstrated schematically in Fig.13.

The resistance curves needed are given in Fig.14, while the crack driving force curves are determined through 3D finite element analyses described in section 4.2. Assessment results of tensile strain capacity for 5 different crack lengths are given in Fig. 14 (a) to Fig. 14 (f). It can be concluded from Fig. 14 that the tensile strain capacity gets smaller as the crack length rises.

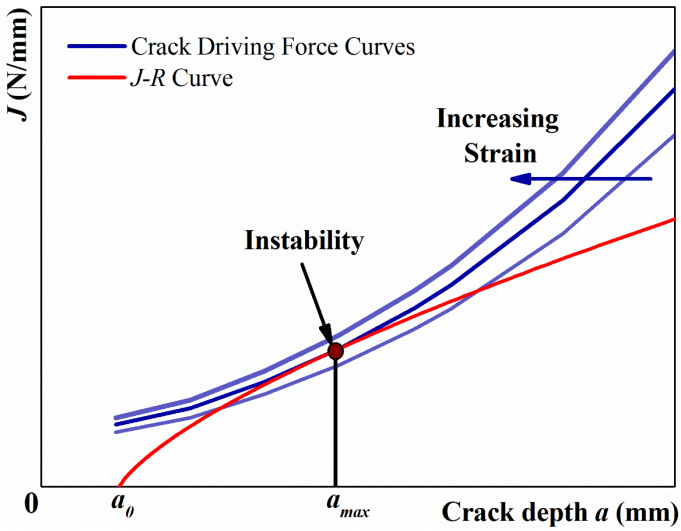

Fig. 13 Illustration of the tangent method.

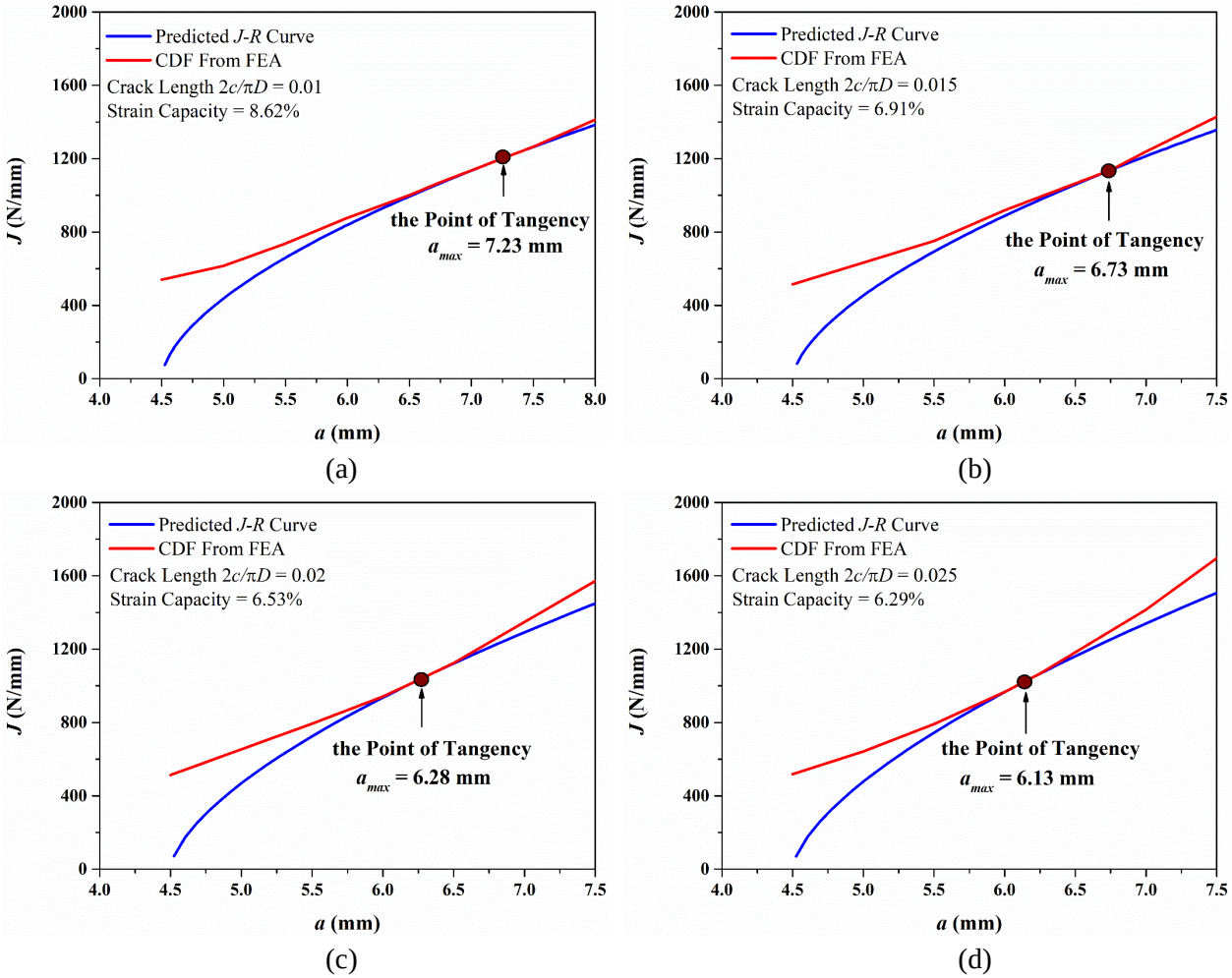

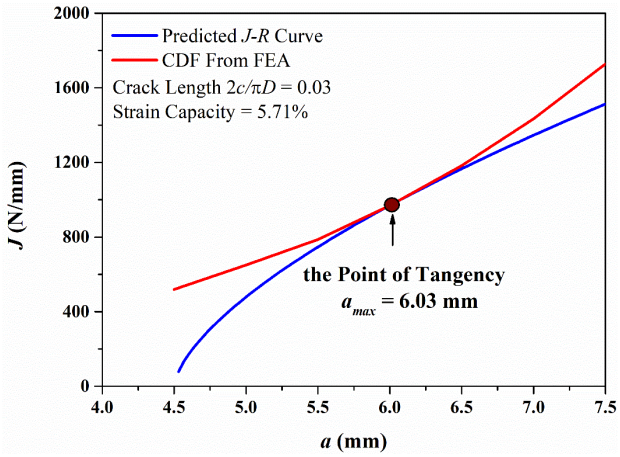

(e)

Fig. 14 Maximum allowable crack depths and tensile strain capacity obtained based on predicted *J-R* curves with different crack lengths: $2c/\pi D$ = 0.01 (a); $2c/\pi D$ = 0.015 (b); $2c/\pi D$ = 0.02 (c); $2c/\pi D$ = 0.025 (d); $2c/\pi D$ = 0.03 (e).

6.3 Comparison with the ExxonMobil strain-based engineering critical assessment method

Recently, ExxonMobil developed a tensile strain capacity (TSC) prediction approach using the Gurson-Tvergaard-Needleman (GTN) model to represent the ductile tearing processes [42]. A serial TSC analytical equation was developed and validated against 93 full-scale tests, which is applicable to a broad range of pipe grades, geometries, material properties and flaw sizes. Therefore, the present tensile strain capacity (TSC) prediction approach is compared with ExxonMobil as shown in Fig. 15. Compared with the strain capacity predicted by a_0/W = 0.25, ExxonMobil gives a non-conservative result when the crack length $2c/t$ is shorter than 3.0. The strain capacity predicted by ExxonMobil is approximately 20% larger than those determined through FEA. As the crack gets longer, the maximum allowable strain become smaller, and the distinction between two results becomes negligible. Moreover, compared with strain capacity predicted by a_0/W = 0.30 and 0.35, the result by the present work are slightly higher for shorter cracks. However, when the crack length $2c/t$ becomes larger than 3.0, the assessment result predicted by ExxonMobil is smaller than that by FEA under all circumstances, indicating that ExxonMobil gives more conservative results for longer

cracks. Although some discrepancy still exists, a relatively good agreement in terms of TSC between the present work and ExxonMobil can be achieved.

To the knowledge of the authors, the difference between two methods can be attributed to the following reasons: Firstly, the pipeline models used to formulate and validate the ExxonMobil TSC equation have a larger wall thickness to diameter ratio *t/D* than the model used in this article, which may be a breach of the equation to some extend; moreover, a larger ratio *t/D* of pipeline tends to increase stress intensity factor and crack driving force, and thus leads to a conservative strain capacity assessment result; Secondly, the mechanical property of the pipelines applied in the study is beyond the limit of the ExxonMobil equation. Finally, the damage mechanics model in the ExxonMobil is the standard Gurson-Tvergaard-Needleman (GTN) model where the damage growth or material softening in pure shear cannot be predicted. Therefore, due to the complex physics, potentially interacting variables and inherent data scatter, comprehensive validation is still necessary to ensure the accuracy and robustness of the predictive models.

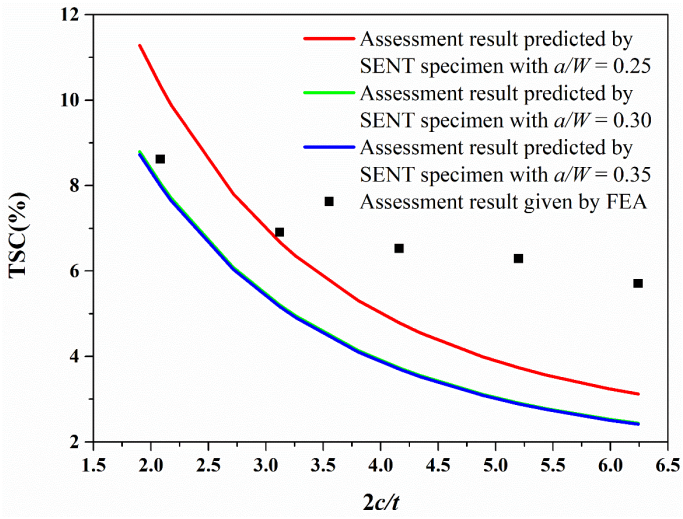

Fig. 16 Comparison of tensile strain capacity (TSC) between the present study and ExxonMobil model.

7 Conclusions

In the study, a methodology is proposed based on clamped SENT experiments and crack-tip constraints theory to predict the fracture response of a full-scale cracked pipe with girth weld:

a) the experiments on SENT specimens with seven different crack depths and four different thickness to width ratios are carried out to study the effect of both in-plane and out-of-plane constraints. Results show resistance curves exhibit great dependency on geometrical dimensions, namely, the crack tip constraint effect. Specimen that has a shallower crack and a thinner thickness always produce higher *J-R* curve;

b) Based on the out-of-plane extension of bending modified *J-Q* theory and the bending modified *J-Q* theory, a mathematical expression representing a family of the constraint corrected *J-R* curves is constructed for X80 weld joint. Through validation and comparison against the J-A_2 constraint modified *J-R* curves, the newly developed Q_m-Q_z constraint-modified *J-R* curve is proven more reliable for a wide range of crack length;

c) the extrapolated resistance curves from SENT to full-scale X80 welded pipes with internal surface cracks are used to demonstrate its application in the strain-based fracture assessment. The tensile strain capacity (TSC) corresponding to the critical crack lengths are determined by tangency approach using the predicted *J-R* curve and the crack driving force from the finite element analyses. For comparison, the ExxonMobil strain-based engineering critical assessment approach, the tensile strain capacity for the cracked X80 pipelines are obtained. At final, a good agreement between the present work and the ExxonMobil result can be achieved in terms of TSC vs. crack length.

Acknowledgements

The authors are grateful for the supports provided by the National Natural Science Foundation of China

(Grant No. 52075366).

References

[1] P.J. Budden, R.A. Ainsworth, The shape of a strain-based failure assessment diagram, Int. J. Press. Vessel. Pip. 89 (2012) 59–66. https://doi.org/10.1016/J.IJPVP.2011.09.004.

[2] P.J. Budden, M.C. Smith, Numerical Validation of a Strain-Based Failure Assessment Diagram Approach to Fracture, Am. Soc. Mech. Eng. Press. Vessel. Pip. Div. PVP. 6 (2010) 1797–1806. https://doi.org/10.1115/PVP2009-77377.

[3] H.A. Bratfos, Use of strain-based ECA for the assessment of flaws in pipeline girth welds subjected to plastic deformations, in: Int. Conf. Appl. Eval. High Grade Linepipes Hostile Environ. Yokohoma, Japan, Nov, 2002: pp. 8–9.

[4] Y.-Y. Wang, D. Rudland, R. Denys, D. Horsley, A Preliminary Strain-Based Design Criterion for Pipeline Girth Welds, Proc. Int. Pipeline Conf. IPC. A (2009) 415–427. https://doi.org/10.1115/IPC2002-27169.

[5] E. Østby, K.R. Jayadevan, C. Thaulow, Fracture response of pipelines subject to large plastic deformation under bending, Int. J. Press. Vessel. Pip. 82 (2005) 201–215. https://doi.org/10.1016/j.ijpvp.2004.08.012.

[6] Y. Huang, W. Zhou, E. Wang, Constraint-corrected J-R curve based on three-dimensional finite element analyses, Fatigue Fract. Eng. Mater. Struct. 37 (2014) 1101–1115. https://doi.org/10.1111/ffe.12190.

[7] K. Minnaar, P.C. Gioielli, M.L. Macia, F. Bardi, N.E. Biery, W.C. Kan, Predictive FEA Modeling of Pressurized Full-Scale Tests , (2007).

[8] E. Østby, A.O. Hellesvik, Fracture Control – Offshore Pipelines JIP Results From Large Scale Testing of the Effect of Biaxial Loading On the Strain Capacity of Pipes With Defects , (2007).

[9] S. Igi, N. Suzuki, Tensile Strain Limits of X80 High-strain Pipelines , (2007).

[10] DNVGL-RP-F108, Assessment of flaws in pipeline and riser girth welds, Det Norske Veritas, Norway, (2017).

[11] BS 8571, Method of test for determination of fracture toughness in metallic materials using single edge notched tension (SENT) specimens, British Standards Institution, London, (2018).

[12] ASTM E1820-20b, Standard test method for measurement of fracture toughness, American Society for Testing and Materials, (2020).

[13] D.Y. Park, W.R. Tyson, J.P. Gravel, CANMET SENT test method, updates and applications, Int. J. Press. Vessel. Pip. 156 (2017) 8–16. https://doi.org/10.1016/j.ijpvp.2017.07.002.

[14] BS 7448-1, Fracture mechanics toughness tests. Method for determination of KIc, critical CTOD and critical J values of metallic materials, British Standards Institution, London, (1991).

[15] ISO 12135:2016, Unified method of test for the determination of quasistatic fracture toughness, International Organization for Standardization, (2016).

[16] M. Panico, H. Tang, D.P. Fairchild, W. Cheng, ExxonMobil SENT test method and application to Strain-Based Design, Int. J. Press. Vessel. Pip. 156 (2017) 17–22. https://doi.org/10.1016/J.IJPVP.2017.06.010.

[17] S. Cravero, C. Ruggieri, Estimation procedure of J-resistance curves for SE(T) fracture specimens using unloading compliance, Eng. Fract. Mech. 74 (2007) 2735–2757. https://doi.org/10.1016/J.ENGFRACMECH.2007.01.012.

[18] S. Cravero, C. Ruggieri, Further developments in J evaluation procedure for growing cracks based on

LLD and CMOD data, Int. J. Fract. 2008 1484. 148 (2008) 387–400. https://doi.org/10.1007/S10704-008-9211-9.

[19] M.A. Verstraete, S. Hertelé, R.M. Denys, K. Van Minnebruggen, W. De Waele, Evaluation and interpretation of ductile crack extension in SENT specimens using unloading compliance technique, Eng. Fract. Mech. 115 (2014) 190–203. https://doi.org/10.1016/j.engfracmech.2013.11.004.

[20] DNVGL-OS-F101, Submarine pipeline systems, Det Norske Veritas, Norway, (2013).

[21] Z. Liu, X. Wang, J. Tang, C. Deng, H. Zhao, X. Chen, The effects of in-plane and out-of-plane constraints on J-R curves for X80 steel: A study using clamped SENT specimens, Eng. Fract. Mech. 206 (2019) 342–358. https://doi.org/10.1016/j.engfracmech.2018.12.004.

[22] P.-S. Lam, Y.J. Chao, X.-K. Zhu, Y. Kim, R.L. Sindelar, Determination of Constraint-Modified J-R Curves for Carbon Steel Storage Tanks , J. Press. Vessel Technol. 125 (2003) 136–143. https://doi.org/10.1115/1.1564069.

[23] Y.J. Chao, X.K. Zhu, Constraint-modified J−R curves and its application to ductile crack growth, Int. J. Fract. 106 (2000) 135–160. https://doi.org/10.1023/A:1007638400006.

[24] Y. Li, B. Gong, M. Corrado, C. Deng, D. Wang, Experimental investigation of out-of-plane constraint effect on fracture toughness of the SE(T) specimens, Int. J. Mech. Sci. 128–129 (2017) 644–651. https://doi.org/10.1016/j.ijmecsci.2017.06.002.

[25] E. Wang, W. Zhou, G. Shen, Three-dimensional finite element analysis of crack-tip fields of clamped single-edge tension specimens - Part II: Crack-tip constraints, Eng. Fract. Mech. 116 (2014) 144–157. https://doi.org/10.1016/j.engfracmech.2013.10.023.

[26] K. Lu, T. Meshii, Three-dimensional T-stresses for three-point-bend specimens with large thickness variation, Eng. Fract. Mech. 116 (2014) 197–203. https://doi.org/10.1016/J.ENGFRACMECH.2013.12.011.

[27] V.N. Shlyannikov, N. V. Boychenko, A. V. Tumanov, A. Fernández-Canteli, The elastic and plastic constraint parameters for three-dimensional problems, Eng. Fract. Mech. 127 (2014) 83–96. https://doi.org/10.1016/J.ENGFRACMECH.2014.05.015.

[28] T. Meshii, K. Lu, Y. Fujiwara, Extended investigation of the test specimen thickness (TST) effect on the fracture toughness (Jc) of a material in the ductile-to-brittle transition temperature region as a difference in the crack tip constraint − What is the loss of constraint in the TST effects on Jc?, Eng. Fract. Mech. 135 (2015) 286–294. https://doi.org/10.1016/J.ENGFRACMECH.2014.07.025.

[29] S. Yang, Y.J. Chao, M.A. Sutton, Higher order asymptotic crack tip fields in a power-law hardening material, Eng. Fract. Mech. 45 (1993) 1–20. https://doi.org/10.1016/0013-7944(93)90002-A.

[30] Y.J. Chao, S. Yang, M.A. Sutton, On the fracture of solids characterized by one or two parameters: Theory and practice, J. Mech. Phys. Solids. 42 (1994) 629–647. https://doi.org/10.1016/0022-5096(94)90055-8.

[31] S. Yang, Y.J. Chao, M.A. Sutton, Complete theoretical analysis for higher order asymptotic terms and the HRR zone at a crack tip for Mode I and Mode II loading of a hardening material, Acta Mech. 98 (1993) 79–98. https://doi.org/10.1007/BF01174295.

[32] X.K. Zhu, B.N. Leis, Bending modified J-Q theory and crack-tip constraint quantification, Int. J. Fract. 141 (2006) 115–134. https://doi.org/10.1007/s10704-006-0068-5.

[33] C.F. Shih, Tables of Hutchinson-Rice-Rosengren singular field quantities. Report MRL E-147, Mater. Res. Lab. Brown Univ. Provid. (1983).

[34] B. Gong, C. Xia, G. Lacidogna, Q. Xu, Y. Liu, Y. Li, Constraint analysis of thickness effects on fracture resistance behavior of clamped single-edge notch tension specimen, Theor. Appl. Fract. Mech. 110 (2020) 102802. https://doi.org/10.1016/j.tafmec.2020.102802.

[35] W. Guo, Elastoplastic three dimensional crack border field-I. Singular structure of the field, Eng. Fract. Mech. 46 (1993) 93–104. https://doi.org/10.1016/0013-7944(93)90306-D.

[36] W. Guo, Elastoplastic three dimensional crack border field-II. Asymptotic solution for the field, Eng. Fract. Mech. 46 (1993) 105–113. https://doi.org/10.1016/0013-7944(93)90307-E.

[37] ASTM E8/E8M-16a: Standard Test Methods for Tension Testing of Metallic Materials, American Society for Testing Materials, USA, (2016).

[38] M.R. Mitchell, R.E. Link, G. Shen, W.R. Tyson, Crack Size Evaluation Using Unloading Compliance in Single-Specimen Single-Edge-Notched Tension Fracture Toughness Testing, J. Test. Eval. 37 (2009) 102368. https://doi.org/10.1520/JTE102368.

[39] G. Shen, J.A. Gianetto, W.R. Tyson, Measurement of J-R curves using single-specimen technique on clamped SE(T) specimens, in: Proc. Int. Offshore Polar Eng. Conf., OnePetro, 2009: pp. 92–99.

[40] J. Yang, G.Z. Wang, F.Z. Xuan, S.T. Tu, Unified correlation of in-plane and out-of-plane constraints with fracture toughness, Fatigue Fract. Eng. Mater. Struct. 37 (2014) 132–145. https://doi.org/10.1111/ffe.12094.

[41] H.S. Zhao, S.T. Lie, Y. Zhang, Strain-based J-estimation scheme for fracture assessment of misaligned clad pipelines with an interface crack, Mar. Struct. 61 (2018) 238–255. https://doi.org/10.1016/j.marstruc.2018.06.006.

[42] H. Tang, D. Fairchild, M. Panico, J. Crapps, W. Cheng, Strain Capacity Prediction of Strain-Based Pipelines, Proc. Bienn. Int. Pipeline Conf. IPC. 4 (2014). https://doi.org/10.1115/IPC2014-33749.